Implementation of Radio-Frequency Deflecting Devices for Comprehensive High-Energy Electron Beam Diagnosis

Paolo Craievich, *Senior Member, IEEE*, Marco Petronio, Sandra G. Biedron, *Senior Member, IEEE*, Davide Castronovo, Massimo Dal Forno, *Member, IEEE*, Simone Di Mitri, Nicolas Faure, Daniele La Civita, Giuseppe Penco, Luca Rumiz, Luca Sturari, Roberto Vescovo, *Member, IEEE*, and Defa Wang

***Abstract*—In next-generation light sources, high-brightness electron beams are used in a free-electron laser configuration to produce light for use by scientists and engineers in numerous fields of research. High-brightness beams are described for such light sources as having low transverse and longitudinal emittances, high peak currents, and low slice emittance and energy spread. The optimal generation and preservation of such high-brightness electron beams during the acceleration process and propagation to and through the photon-producing element is imperative to the quality and performance of the light source. To understand the electron beam's phase space in the accelerating section of a next-generation light source machine, we employed radio-frequency cavities operating in a deflecting mode in conjunction with a magnetic spectrometer and imaging system for both low (250 MeV) and high (1.2 GeV) electron energies. This high-resolution, high-energy system is an essential diagnostic for the optimization and control of the electron beam in the FERMI light source generating fully transversely and longitudinally coherent light in the VUV to soft x-ray wavelength regimes. This device is located at the end of the linear accelerator in order to provide the longitudinal phase space nearest to the entrance of the photon-producing beam-lines. Here, we describe the design, fabrication, characterization, commissioning, and operational implementation of this transverse deflecting cavity structure diagnostic system for the high-energy (1.2 GeV) regime.**

***Index Terms*—Electron accelerators, electron beam deflection, free-electron lasers, particle beam measurements.**

I. Introduction

TRANSVERSE mode radio-frequency (RF) deflectors have been employed in particle accelerators since the early 1960s in high-energy physics machines to assist with pulse selection [1]–[7]. With the advent of new machines, such as next-generation light sources, whose beams have exceedingly short pulse durations and are of high-brightness, these deflectors are now being used to assist with the characterization of the electron beams [8]–[15]. Recently, the first fully coherent high-gain harmonic-generation (HGHG) free-electron laser (FEL), FERMI, has been successfully commissioned from the VUV to soft x-rays, and is now a facility open to scientists and engineers [16], [17]. The FERMI linac is based on a re-configuration and extension of the original, normal-conducting (copper), S-band (2.998 GHz) linear accelerator, and readers can refer to [18] for more details. In order to comprehensively diagnose the transverse time-sliced emittance and energy spread, and the electron bunch length to high resolution, a transverse mode, backward traveling wave RF deflector cavity was designed and implemented to characterize the beam at the end of the FERMI linear accelerator with a high-resolution spectrometer and imaging system [19]. With constraints of limited available space, limited RF power, a fixed RF frequency, and avoiding the beam break-up instability, the implementation of a $2\pi/3$-mode, normal conducting, high-energy RF deflector operating at S-band was realized. Two deflecting cavities have been designed and installed at the end of the FERMI linac, to stretch the beam respectively in the horizontal and in the vertical planes, as shown in the layout sketched in Fig. 1. The vertical deflecting cavity was installed in December 2011 after successful factory acceptance in August 2011, including microwave measurements. The horizontal deflecting cavity was installed in July 2012 after successful factory acceptance. The two cavities are individually powered by the same klystron and an RF switch system is used to choose the deflection plane. The vertical and horizontal high-energy deflectors (HERFDy and HERFDx) are now regularly operating in the FERMI linac-end.

Manuscript received October 29, 2014; revised December 16, 2014; accepted December 16, 2014. Date of publication January 28, 2015; date of current version February 06, 2015. This work was supported by the FERMI project of Elettra-Sincrotrone Trieste S.C.p.A. and in part by the Ministry of University and Research under grants FIRB-RBAP045JF2 and FIRB-RBAP06AWK3.

P. Craievich was with Elettra-Sincrotrone Trieste, 34100 Trieste, Italy. He is with the Paul Scherrer Institute, Villigen-PSI AG 5232, Switzerland (e-mail: paolo.craievich@psi.ch).

M. Petronio was with the Department of Engineering and Architecture, University of Trieste, 34127 Trieste, Italy. He is now with Danieli, 33042 Buttrio (UD), Italy.

S. G. Biedron was with Elettra-Sincrotrone Trieste, 34100 Trieste, Italy. She is now with the Department of Electrical and Computer Engineering, Colorado State University, Fort Collins, CO 80523 USA.

D. Castronovo, S. Di Mitri, G. Penco, L. Rumiz, and L. Sturari are with Elettra-Sincrotrone Trieste, 34100 Trieste, Italy.

M. Dal Forno was with the Department of Engineering and Architecture, University of Trieste, 34127 Trieste, Italy. He is now with theSLAC National Accelerator Laboratory, Menlo Park, CA 94025 USA.

N. Faure is with PMB Alcen, 13790 Peynier, France.

D. La Civita was with Elettra-Sincrotrone Trieste, 34100 Trieste, Italy. He is now with European XFEL GmbH, D-22761 Hamburg, Germany.

R. Vescovo is with the Department of Engineering and Architecture, University of Trieste, 34127 Trieste, Italy.

D. Wang is retired. At the time of this research, the author was with Elettra-Sincrotrone Trieste, 34100 Trieste, Italy.

Color versions of one or more of the figures in this paper are available online at http://ieeexplore.ieee.org.

Digital Object Identifier 10.1109/TNS.2014.2385155

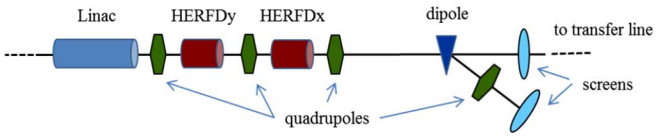

Fig. 1. FERMI linac where the positions of the installed vertical and horizontal high-energy deflectors are indicated by HERFDy and HERFDx, respectively.

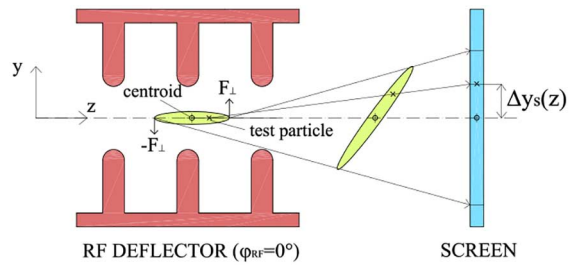

Fig. 2. Deflection of an electron bunch by a transverse deflecting cavity. Note the centroid remains on axis while the front and end of the bunch are spread across the screen as the deflector's force is opposite for the front and end of the bunch.

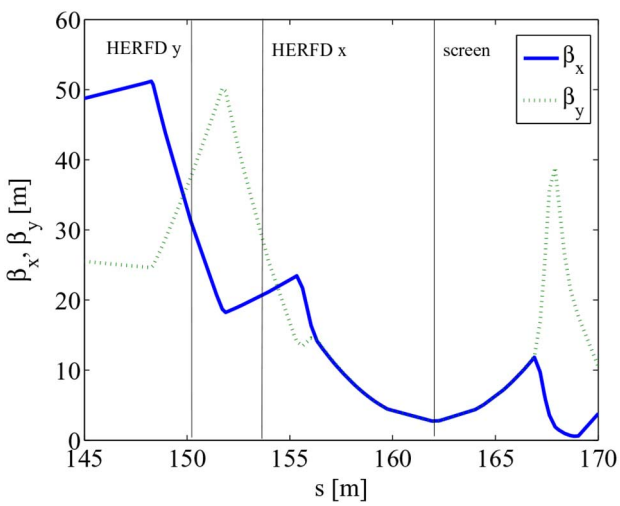

Fig. 3. The beam lattice optics layout for the straight diagnostic section at the linac's end. The locations of the deflectors and screens are highlighted in the plot with vertical lines.

II. Longitudinal and Transverse Phase Space Characterization

The goal of a transverse deflecting cavity is to "stretch" the electron beam in the desired plane as depicted in Fig. 2. When the RF phase is properly set, the deflecting voltage is null in the center of the bunch (centroid) and gives a linear transverse stretching to the head and the tail of bunch. The beam will then strike an optical transition radiation screen whose resultant image (optical signal) can be digitized for subsequent analysis. In this way, the electron beam's longitudinal characteristics are projected into the transverse plane due to the integrated transverse force imparted on the beam by the deflecting cavity. The formulas contained in [10] concerning the dynamics of the bunch deflection as a function of the RF deflector parameters and of the optical parameters are used here. Perturbations to the ideal case due to the finite transverse emittance are also considered. In Fig. 2 the deflecting force imparts a transverse momentum on the bunch with a small kick angle as a function of z, $\Delta y'(z)$, given by

$$\begin{aligned}\Delta y'(z) &= \frac{eV_\perp}{pc}\sin(k_{rf}z+\varphi_{rf}) \\ &\approx \frac{eV_\perp}{pc}\left(k_{rf}z\cos\varphi_{rf}+\sin\varphi_{rf}\right)\end{aligned} \tag{1}$$

where $V_\perp$ is the integrated deflecting voltage, p the beam longitudinal momentum, k_{rf} the free-space wave number, and φ_{rf} the RF phase ($\varphi_{rf}=0$ at zero crossing). We assume that the bunch length is much shorter than the RF wavelength $|z| << 1/k_{rf}$, namely, the kick angle is a linear function of z. Notice that the $k_{rf}\cos\varphi_{rf}$ term in (1) establishes the longitudinal to transverse coordinate correlation; the $\sin\varphi_{rf}$ term refers to the bunch centroid motion and it is null for $\varphi_{rf}=0$. Fig. 3 shows the FERMI beam lattice optics at the end of the linac, including the deflectors and the downstream screen. Table I contains the beam and optical parameters of the diagnostic section at the linac-end that have been used for the calculations in the following paragraphs. The transverse position of each particle at the screen location is then computed through by the transfer matrix element which relates the position at the screen with the particle vertical angular divergence at the deflector, i.e. $R_{34}=\sqrt{\beta_d\beta_s}\sin(\Delta\psi_{ds})$ [20]:

$$\Delta y_S(z)\approx\frac{eV_\perp}{pc}R_{34}\left(k_{rf}z\cos\varphi_{rf}+\sin\varphi_{rf}\right) \tag{2}$$

where β_s and β_d are the vertical beta functions at the deflecting point and the screen locations, respectively, and $\sin(\Delta\psi_{ds})$ is the vertical betatron phase advance from the deflecting point to the screen. In the approximation of null transverse emittance the RMS beam size at the screen is given by

$$\sigma_y=\frac{eV_\perp}{pc}\sigma_z R_{34}k_{rf}\cos\varphi_{rf} \tag{3}$$

where σ_z is the bunch length before the action of the deflection. The transverse centroid offset at the screen is obtained by averaging (2) over z with the assumption of $\langle z\rangle=0$:

$$\langle\Delta y_S\rangle=\frac{eV_\perp}{pc}R_{34}\sin\varphi_{rf}. \tag{4}$$

The calibration factor S is defined as the ratio between the beam spot at the screen (σ_y) and the temporal bunch length (σ_z) and can be written as

$$S=\frac{\sigma_y}{\sigma_t}=\frac{eV_\perp}{pc}ck_{rf}\sqrt{\beta_d\beta_s}\sin(\Delta\psi_{ds}). \tag{5}$$

By using (5), the time resolution of the measurement can be defined as

$$\sigma_{t,R}\geq\frac{\sigma_{y0}}{S}=\sqrt{\frac{\varepsilon_{N,y}}{\gamma\beta_d}}\frac{pc}{eV_\perp}\frac{1}{ck_{rf}\sin(\Delta\psi_{ds})} \tag{6}$$

where $\varepsilon_{N,y}$ is the normalized beam vertical emittance, γ is the Lorentz factor, and σ_{y0} is the natural transverse beam size (i.e.,

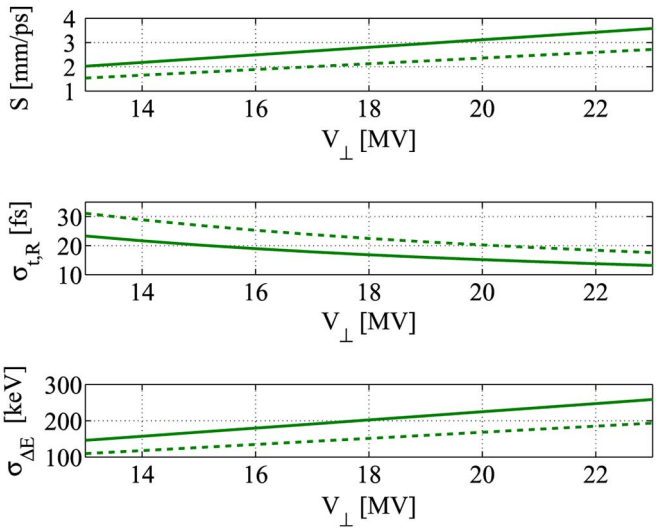

Fig. 4. Calibration factors S, time resolutions $\sigma_{t,R}$, and induced energy spread $\sigma_{\Delta E}$ as a function of the integrated deflecting voltage $V_\perp$ for the HERFDy (solid line) and the HERFDx (dashed line).

without the transverse deflection). However, as described in [21] and [22], an RF deflecting device induces an additional energy spread proportional to the deflecting voltage, according to the following formula:

$$\sigma_{\Delta E} \geq \frac{\varepsilon_{N,y} E_0}{\sin(\Delta\psi_{ds}) c \sigma_{t,R}} \tag{7}$$

where $E_0 = m_e c^2 \approx 511$ keV is the electron rest energy. Fig. 4 shows calibration factors, the time resolutions and induced energy spread as a function of the integrated voltage for both deflectors, obtained by using parameters listed in Table I and considering a beam energy of 1.2 GeV. The measurements of the bunch length and of the current profile can be readily obtained from the combination of a transverse deflector device and a screen. The particles along the bunch enter the deflecting device at different times and therefore each experiences a different phase. The difference in phase is dependent upon its position along the bunch and the RF frequency. The electrons along the bunch that are within the linear position of the RF wave are now spread out into the transverse space (x or y, depending upon the orientation of the deflector device) proportional to their former positions in longitudinal space. Considering a realistic bunch with a finite transverse emittance, after deflection, the rms beam size at the screen can be estimated by the quadratic summation of the natural transverse beam size and the rms beam size at the screen:

$$\begin{aligned} \sigma_y &= \sqrt{\sigma_{y,0}^2 + \sigma_y^2} \\ &= \sqrt{\frac{\varepsilon_{N,y}\beta_s}{\gamma} + \frac{eV_\perp}{pc}\sigma_z R_{34} k_{rf} \cos\varphi_{rf}} \end{aligned} \tag{8}$$

Perturbation due to the finite emittance is negligible if $\sigma_y >> \sigma_{y,0}$. In order to be able to measure a 1.2-GeV, 200 fs-long electron bunch with a resolution of about 15-20 fs rms, in the nominal machine condition of Table I, the integrated voltage should reach 20 MV. In this configuration, the streaked bunch on the screen could be sliced in ten or more time-slices and the implementation of the well known quadrupole-scan technique [23] allows us to measure the beam time-sliced transverse emittance and Courant-Snyder optics parameters.

TABLE I
BEAM AND LATTICE (BEAM OPTICS) PARAMETERS INVOLVED IN THE STREAKING PROCESS FOR THE DIAGNOSTIC SECTION AT THE LINAC-END. THE ELECTRON BEAM ENERGY CAN BE VARIED FROM 1.0 TO 1.5 GEV ACCORDING TO THE FEL WAVELENGTH SETTINGS REQUIRED. TDS: TRANSVERSE DEFLECTING STRUCTURE

Parameter	Symbol	Uncompressed Beam	FEL-1/2	Unit
Beam energy	E	1.0- 1.5	1.0-1.5	GeV
Charge	Q	800	800	pC
β_x@TDS	$\beta_{d,x}$	21	21	m
β_y@TDS	$\beta_{d,y}$	38	38	m
$\beta_{x,y}$@screen	$\beta_{s,x,y}$	3	3	m
Bunch length	σ_t	3.2	0.2	ps
Emittance (projected)	$\gamma\varepsilon_x$,$\gamma\varepsilon_y$	1.2	2.0	$\mu mrad$

Moreover, the vertical deflector in conjunction with the horizontal spectrometer bending magnet, allows the reconstruction of the longitudinal phase space. In fact, the former induces a correlation between the temporal distribution and the vertical displacement, while the bending magnet chromatically disperses the electrons in the horizontal plane, making the information about the beam energy profile available along that direction. As a consequence the beam longitudinal phase space can be visualized on a fluorescent YAG crystal plus a CCD camera system placed downstream [24], allowing in addition characterization of the relative time-sliced energy spread along the bunch. The horizontal beam size measured after the dipole spectrometer represents the electron energy deviation, which is given by

$$\Delta x = \eta_{x,s}\delta \tag{9}$$

where $\eta_{x,s}$ is the horizontal momentum dispersion function at the screen, and δ is the relative energy deviation before the energy spectrometer. The rms energy spread resolution is defined as

$$\sigma_{E,res} = \frac{\sqrt{\beta_x \varepsilon_x}}{\eta_{x,s}} E. \tag{10}$$

Fig. 5 shows the optics layout of the energy spectrometer beam-line at the linac end. For the nominal lattice with a horizontal dispersion at the spectrometer line screen $\eta_{x,s} = 1.79$ m, the rms energy spread resolution is $\sigma_{E,res} \approx 40$ keV at 1.2 GeV. The screen system resolution is 30 μm/pixel and it approximately corresponds to the minimum rms beam size that can be measured at the screen itself. The screen resolution is comparable to the optical beam size in the spectrometer beam-line, so adding the two contributions in quadrature, we obtain a resolution of about 50 keV. In time-sliced energy spread measurements, it should be considered that off-axis accelerating fields induce an additional energy spread that is inversely proportional to the time resolution, as indicated in (7). Further, in order to diagnose the short bunches required by FERMI, a high longitudinal resolution is required, i.e., a high deflecting voltage, but this consequently leads to a large induced energy spread that

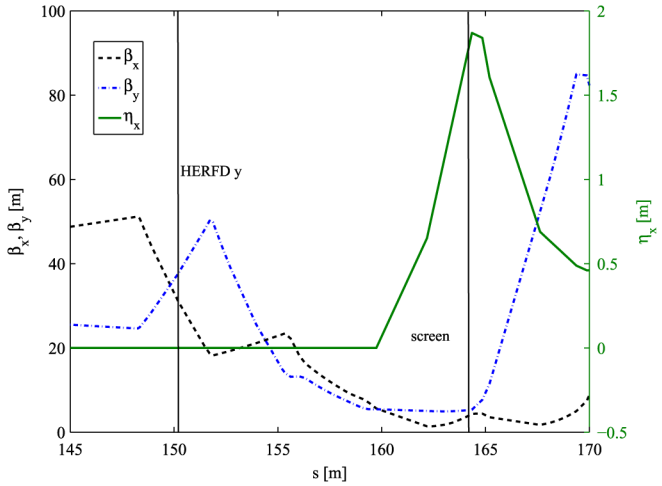

Fig. 5. Optics layout of the energy spectrometer at the linac's end. The locations of the deflectors and screens are highlighted in the plot with vertical lines.

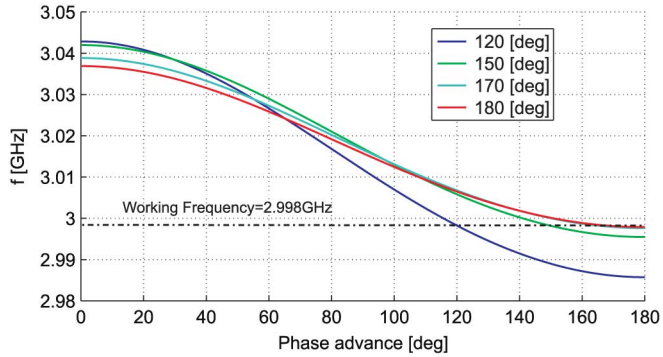

Fig. 6. Dispersion diagram of the three choices considered; each basic cell has been tuned to the working frequency $f_{RF} = 2.998$ GHz. Dispersion diagram of the standing wave π-mode is also plotted for comparison.

limits the energy resolution. For these reasons, the deflecting voltage has to be chosen according to the measurement goal: for the bunch length measurement, the high temporal resolution is preferable despite an eventual energy spread increase, while for the slice energy spread, it is better to operate with a lower deflecting voltage. Also, concerning the longitudinal phase space measurement, the deflector has to be operated with the best compromise between the minimization of its effect on the energy spread and a good temporal resolution.

III. High Energy Deflector Design

A. RF Design

As in the design of the diagnostic systems in numerous accelerators, the diagnostic is constrained by the overall accelerator machine design, not the contrary. We were constrained by several factors: frequency of the available microwave sources (European S-band, 2.998 GHz), the available space in the high-energy region of the linear accelerator ($\leq$ 2.5 m for each deflector), a available RF power of 15 MW, a filling time of the RF structure of $\leq$ 2 μs (the length of the RF pulse). As mentioned in the previous section, the integrated deflecting voltage is required to be larger than 20 MV, in order to reach the required time resolutions for the beam parameters. We therefore required a compact and high-impedance deflector.

It is worthwhile noting that due to the linear accelerator frequency an S-band RF deflector is investigated in this paper over an X-band or C-band deflectors, because it resulted to be able to guarantee the specified deflecting voltage and resolution. By the way, for higher-energy and shorter electron beam, other solutions are available at different frequency, such as X-band and C-band RF deflectors developed at SLAC [25], Radiabeam [26] and RIKEN/Spring-8 [27]. In a traveling wave structure with constant impedance, the integrated deflecting voltage is given by

$$V_{\perp} = \sqrt{2\alpha l}\left(\frac{1-e^{-\alpha l}}{\alpha l}\right)\sqrt{P_{RF} r_t l} = k_D l \sqrt{P_{RF}} \qquad (11)$$

where α is the field attenuation constant, r_t is the transverse shunt impedance per unit length, l is the deflector length, and k_D is the power-to-voltage parameter. In order to meet the specification of the deflecting voltage, and the constraint of the available RF power and space, the power-to-voltage parameter should be greater than 2.1 MV/m/$\sqrt{MW}$. Considering an available space of 2.5 m, the existing S-band deflector structures as LOLA [28], [29] and CERN III [30] have too low k_D values, and precisely $k_D = 1.7$ MV/m/$\sqrt{MW}$ and $k_D = 1.6$ MV/m/$\sqrt{MW}$, respectively; thus it has been necessary a new design. We compared the performance of three traveling wave options to satisfy our RF and space constraints. We examined three different constant impedance modes—the $2\pi/3$ (120 degrees), $5\pi/6$ (150 degrees), and the quasi π (170 degrees) and, for all cases, sensitivity analysis and other relevant RF parameters were examined and scrutinized. The basic individual cavity was designed using the HFSS electromagnetic code [31]. The cell parameters for every choice are the cell length L, the iris radius a, the cell maximum internal radius b, and the iris thickness t. For every configuration, L has been chosen in order to achieve the synchronism condition between the electromagnetic field and the electrons traveling at the speed of light c. The iris radius and the thickness radius have to be $a = 12.5$ mm and $t = 8$ mm, respectively, for each option. The maximum internal radius b has been varied with the code to tune the cell to the working frequency. The dispersion diagram of the three structure options that we have considered is plotted in Fig. 6. Dispersion diagram of the standing wave π-mode is also plotted for comparison. By differentiating (11) with respect to αl, we find that the maximum deflecting efficiency is obtained for $(\alpha l)_{opt} = 1.26$, as for the constant impedance traveling wave accelerating structure. We cannot increase the deflector length l, as we have a space constraint of maximum 2.5 m for each deflector. Since the group velocity v_g is related to the attenuation by $\alpha = \pi f/Qv_g$ where Q is the quality factor, we can instead optimize the deflecting mode to find the ideal deflector efficiency by reducing v_g. To do so, we could not exceed the RF pulse length, t_{RF}, that constrains the filling time of the traveling wave structure, given by $t_f = l/v_g$. To achieve the desired deflecting voltage of 20 MV:

- for the $2\pi/3$ option: 62 cells and a total deflector length of 2.066 m;

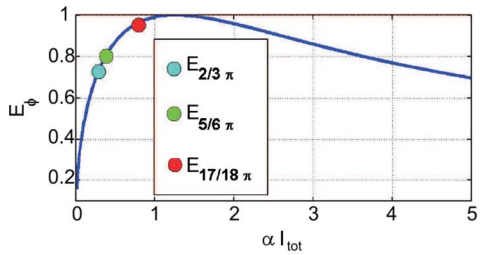

Fig. 7. Efficiency of the three traveling mode deflector options $2\pi/3$ (Aqua), $5\pi/6$ (Green), and $17\pi/18$ (Red), plotted with the normalized theoretical deflecting voltage (blue line).

TABLE II
RESULTING RF PARAMETERS FOR THE $2\pi/3$, $5\pi/6$ AND $17\pi/18$ OPTIONS TO REACH AN INTEGRATED DEFLECTING VOLTAGE OF 20 MV

	$2\pi/3$	$5\pi/6$	$17\pi/18$	**Unit**
L	33.33	41.66	47.22	mm
b	59.33	59.52	59.66	mm
l	2.066	1.750	1.369	m
Q	13500	15800	17200	
r_t	29.9	29.5	26.7	$M\Omega/m$
α	0.147	0.221	0.594	Np/m
β_g	-1.580	-0.895	-0.308	%
t_f	0.43	0.65	1.48	μs

- for the $5\pi/6$ option: 42 cells and a total deflector length of 1.75 m;
- for the quasi π ($17\pi/18$) option: 29 cells and a total deflector length of 1.369 m.

The simulated RF parameters determined for all three cases are listed in Table II. We next compared the modes in terms of efficiency. The mode efficiency is given by

$$E_\phi = \frac{V_t(\alpha l)_\phi}{V_t(\alpha l)_{opt}} \tag{12}$$

where $\phi = 2\pi/3$, $5\pi/6$, and $17\pi/18$. E_ϕ is represented in Fig. 7. The slowest mode ($17\pi/18$) has the best efficiency, very near to the maximum theoretical deflector efficiency achievable. Mostly important is that all three modes satisfy the requirement that the filling time is smaller than the available RF pulse length.

Next, we evaluated the sensitivities obtained analyzing the basic cell for every option and we found that the external cell radius and iris radius are by far the most sensitive parameters. The frequency sensitivities are reported in Table III. Concerning the frequency sensitivities relative to the external cell radius it is possible to conclude that errors in the cell diameter machining of the order of ± 10 μm give frequency errors of the order of ∓ 240 kHz. A cell with a relative frequency error $\partial f/f$ gives an additional phase advance shift for cell $\partial\phi/\phi_0 = 1/\beta_g \partial f/f$ and as a result, the wave phase velocity will differ from the beam velocity. Under these assumptions, phase advance errors in the single cell are $\pm 0.6°$, $\pm 1.3°$ and $\pm 4.4°$ for the $2\pi/3$, $5\pi/6$ and $17\pi/18$, respectively. Based on the mechanical tolerance, we therefore chose to proceed with the $2\pi/3$ option. We selected an iris-loaded backward traveling structure with a uniform cell geometry and identical parameters for each cell, namely, a constant-impedance type, in consideration of its development period and structure simplicity. In order to take into account effects of the mechanical tolerance on the integrated deflecting voltage, our $2\pi/3$ mode backward traveling deflecting device in practice is composed of 72 basic cells and two additional couplers at the structure's input and output. The basic cells are mainly magnetically coupled on axis and the input and output cavities are specifically designed to match the structure to the RF source and load. A schematic view of the overall deflector concept is shown in Fig. 8. The brazing process and geometrical imperfections can however give variations of the structure's dimension and therefore frequency error in each cell. Frequency tuning is obtained by introducing two deformations placed in each cell in the diametrically opposite position relative to the axis of the structure. Electromagnetic simulation of two spherical deformations with a diameter of 2 mm shows the frequency increasing by 1.4 MHz, enough to compensate frequency errors due to limited precision in the cell production.

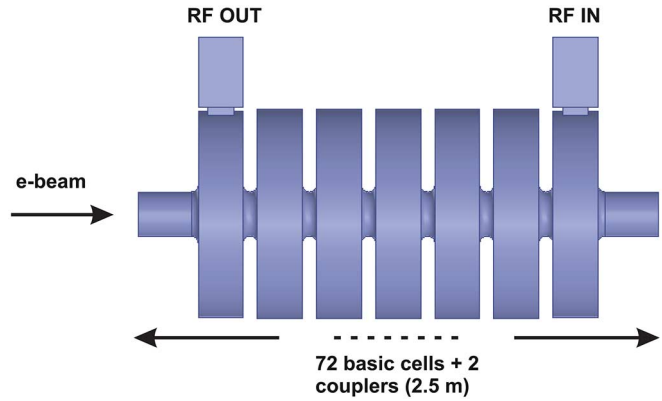

Fig. 8. Sketch of the high-energy RF deflector.

TABLE III
RESULTS OF BASIC CELL SENSITIVITY STUDIES FOR THE STUDIED OPTIONS

	$2\pi/3$ [MHz/mm]	$5\pi/6$ [MHz/mm]	$17\pi/18$ [MHz/mm]
$\partial f/\partial a$	-16.4	-15.4	-14.4
$\partial f/\partial b$	-48.6	-48.4	-48.0
$\partial f/\partial L$	2.6	1.7	1.4
$\partial f/\partial t$	-2.4	-1.0	-0.6

B. Mode-Separation

The dipole deflecting mode has two degenerating polarizations, and in order to avoid the excitation of the mode with polarity rotated at 90°, two longitudinal rods of diameter 3 mm crossing the cells off-axis at 50 mm were inserted. Basically the working frequency of the deflecting mode with polarity at 0° is essentially unperturbed, while the frequency shift of the 90° polarization is about 120 MHz. Fig. 9 shows the HFSS simulations on the pass-bands of the horizontal and vertical polarizations, where the vertical mode has still a wide pass-band of 423 MHz, resulting in clear mode-separation, high group-velocity, and low sensitivity to fabrication tolerances.

C. Input and Output Coupler

In the traveling wave structures, a proper coupler design is required to correctly excite the periodic field inside the cavity,

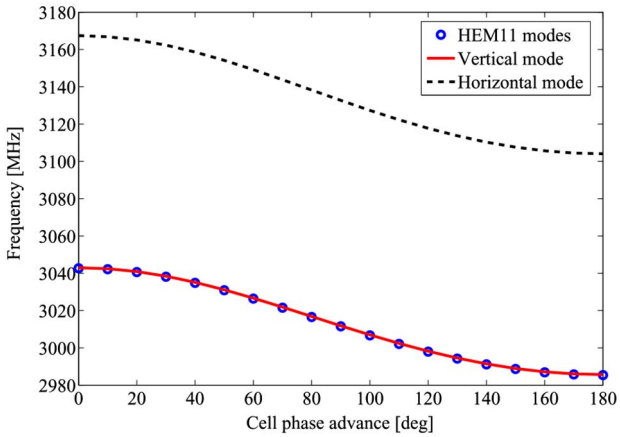

Fig. 9. Pass-band of the HEM11 polarizations before and after splitting with the two longitudinal rods.

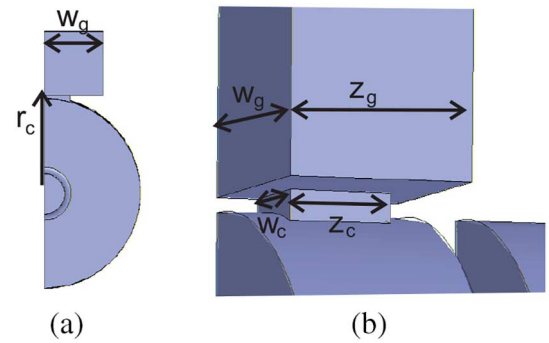

Fig. 10. Detail of the coupler of the traveling wave deflector. Geometrical parameters are $w_g = 72.14mm$, $z_g = 25.33mm$, $z_c = 14.4mm$, window thickness 2 mm, $r_c = 58.36mm$, and $w_c = 17.14mm$.

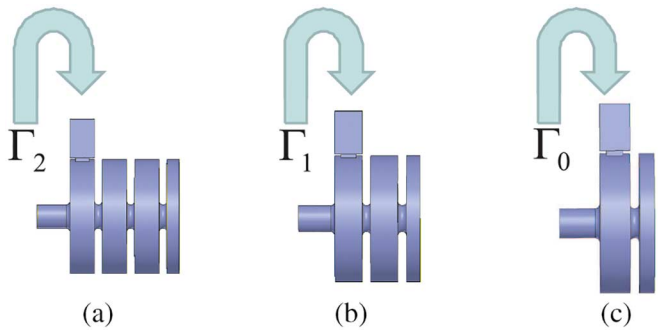

Fig. 11. Short-circuit model used to excite the $2\pi/3$ mode in the traveling-wave deflector.

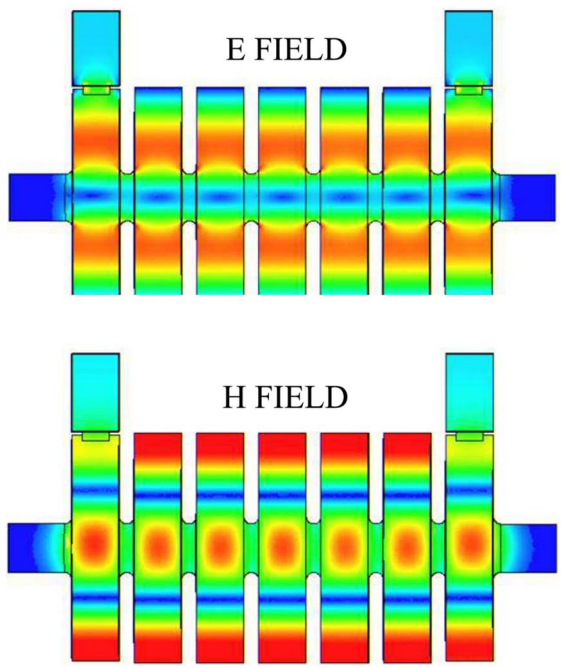

Fig. 12. 2-D distribution of the complex magnitude of the magnetic and electric fields computed in the seven cell structure.

while minimizing the reflection coefficient. The phase advance must be 120 degrees at the working frequency of 2998.01 MHz. The coupler matching is achieved with a trial-and-error procedure, by varying the coupler radius r_c, and the width w_c of the coupling window, both shown in Fig. 10, according to the short-circuits method reported in the references [32]. It can be shown that a necessary and sufficient condition to obtain critical coupling (reflection coefficient $\Gamma = 0$) and the correct phase advance ϕ between the cells is given by

$$\begin{cases} \alpha & = \angle\frac{\Gamma_1}{\Gamma_0} & = -2\varphi \\ \beta & = \angle\frac{\Gamma_2}{\Gamma_1} & = -2\varphi \end{cases} \tag{13}$$

where Γ_i for i $= 2, 1, 0$ denotes the phase of the reflection coefficients evaluated with the model shown in Fig. 11(a), (b), and (c), respectively. Once the condition in (13) is met, where $\phi = 2\pi/3$ in our case, the coupler satisfies the critical coupling and excites the correct phase advance independently of the number of cells in the periodic structure. We have obtained the critical coupling, $|\Gamma| \leq 0.02$, with $r_c = 58.36$ mm and $w_c = 17.14$ mm. It is worthwhile noting that a taper between the WR284 standard waveguide and the coupler waveguide is used in order to adapt the different waveguide dimensions.

In order to validate the performance of the couplers, we simulated seven cells, including the two coupler cells, and analyzed the electric field and magnetic field components as shown in Fig. 12. The chosen geometry keeps the maximum surface electric field at 20.5 MV/m and the maximum magnetic field at 110 kA/m at the coupler window. These field values are low enough to keep the temperature rise due to pulse heating below 5°K. Defining $E_{y,n} = qE_y/max(qcB_x/\mu)$ and $H_{x,n} = (qcB_x/\mu)/max(qcB_x/\mu)$, the normalized components to the Lorentz force with respect to the magnetic component, we have evaluated $E_{y,n}$, $H_{x,n}$, and $E_{y,n} + H_{x,n}$ on the z-axis in Fig. 13. The magnetic field gives the most relevant contribution of the deflection. This is in agreement with the fact that for an iris of $a = 12.5$ mm, the group velocity is negative, which means that the coupling between the deflector cells is mostly magnetic. Fig. 13 also shows that the electric field has a peak in the middle of the iris, while the magnetic field has a peak in the middle of the cell. In Fig. 14, the phase of E_x and H_y along the seven-cell deflector are plotted. The phase advance is periodic with $\phi = 120$ deg and the phases of E_x and H_x are flat in the middle of the iris and in the middle of the cell, respectively.

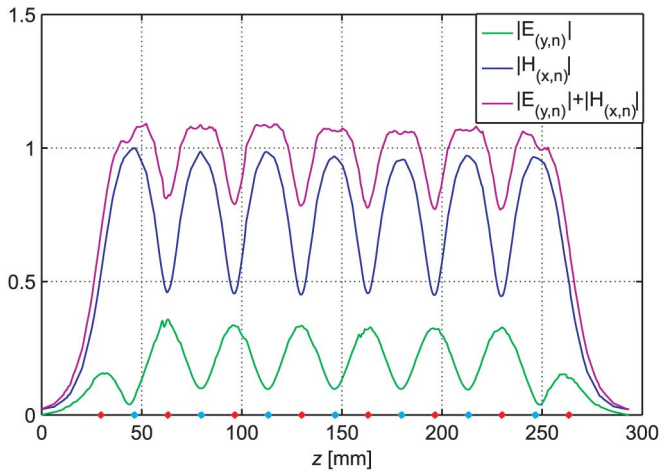

Fig. 13. Simulated $E_{y,n}$, $H_{x,n}$, and $E_{y,n} + H_{x,n}$ on the z axis as a function of the longitudinal deflector coordinate; the red and the blue points on the z axis represent the middle of the iris and the middle of the cells, respectively.

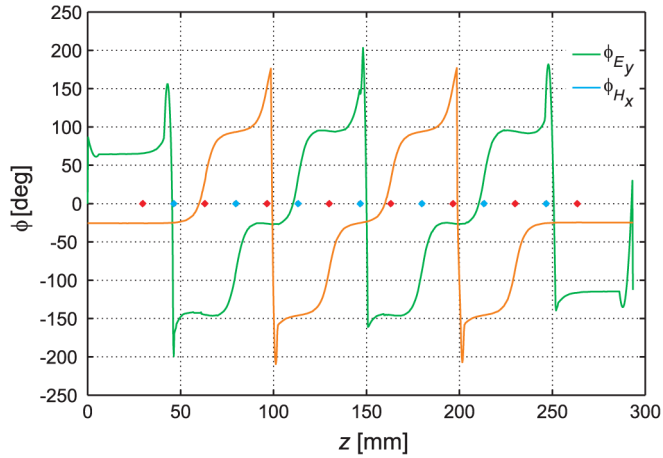

Fig. 14. Simulated phase advance ϕ_{Ey} and ϕ_{Hx} as a function of the longitudinal deflector coordinate z; the red and the blue points represent the middle of the iris and the middle of the cells, respectively.

IV. Engineering and Cold RF Measurements

After the RF design and the beam dynamics simulations confirmed the expected performance, we competitively tendered and procured the fabrication of the two high-energy deflectors with the firm PMB High Tech Devices in France, the successful bidder according to the European Union regulations. The main parameters for the specifications are summarized in Table IV, based on a normalized projected emittance of 2 μm at 1.2 GeV. The potential temporal resolution is less than 20 fs rms for both deflectors. Fig. 15 shows the deflector, which is composed by seventy-two cells plus two couplers, which vertically excite the deflecting field. We performed the cold microwave measurements in a clean room with a humidity of 50%, a temperature of 20.2°C, and an atmospheric pressure of 760 Torr. After tuning each cell in the traveling-wave mode and matching the couplers to the whole structure, the $2\pi/3$ mode working frequency of the structures was estimated by phase measurements along the cell's axis, performed by using a rod acting as a short circuit [33]. This movable metal rod allows, measure of the phase advance by shorting each individual cell, step by step. The frequency for which the phase dispersion was less than $\pm 1.0°$ over the full length of the structure was considered as the working frequency. Results of the phase advance measurements are shown in Figs. 16 and 17. The magnitude field measurements are shown in Fig. 18. Table V lists the RF parameters of the vertical and horizontal deflectors, respectively, measured before and after brazing. Due to initial difficulties in the tuning of the vertical deflector, there is a difference of 460 kHz in the operational frequencies between the two deflectors. The quality factor increases after the brazing process, due to the soldering material that improved the electric contact between the cells. It is worthwhile to note that working temperatures for the vertical and horizontal deflectors in the operation conditions are 40.5°C and 31.2°C, respectively. The RF measurements are in excellent agreement with the design points as the specification for the attenuation and filling time do not take into account the waveguide and the aperture of both couplers. After the RF cold test, we performed the vacuum and water channel experiments/measurements of the device.

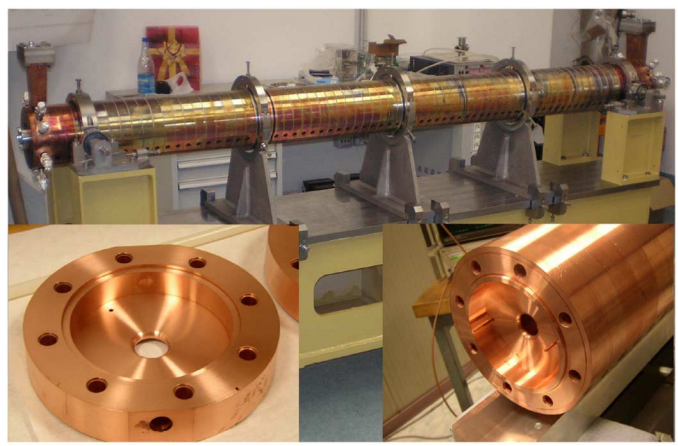

Fig. 15. High-energy deflector composed of seventy-two cells plus two couplers. Basic cell (left) and detail of the two longitudinal rods (right).

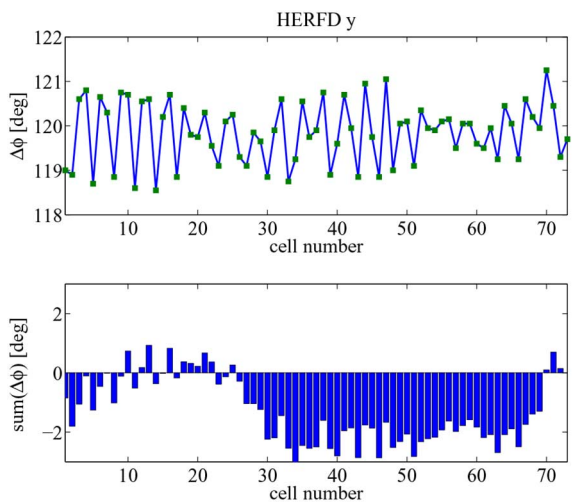

Fig. 16. Results of the phase advance measurements using a movable metallic rod for the vertical (up) deflector, obtaining $\Delta\varphi = 119.9 \pm 0.7 deg(RMS)$ and the integrated phase errors as a function of the cell number (bottom).

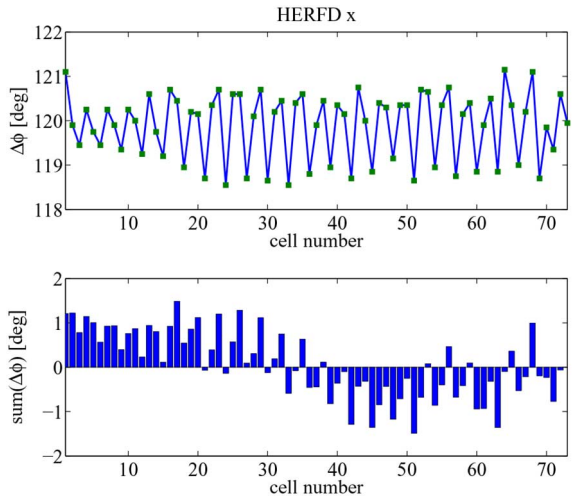

Fig. 17. Results of the phase advance measurements using a movable metallic rod for the horizontal (up) deflector, obtaining $\Delta\varphi = 119.9 \pm 0.7 deg(RMS)$ and the integrated phase errors as a function of the cell number (bottom).

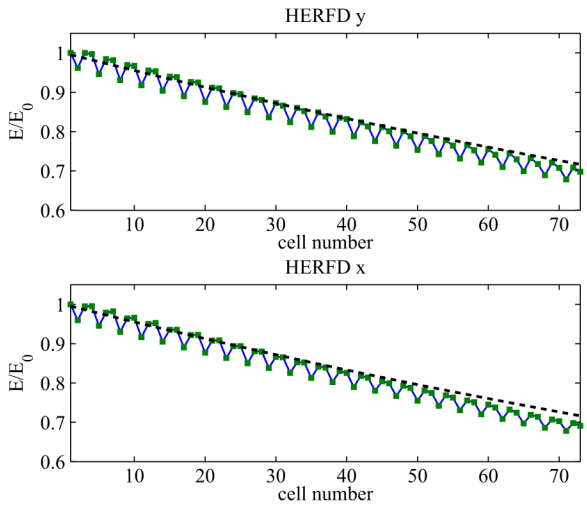

Fig. 18. Results of the field amplitude measurements using a movable metallic rod for the horizontal (up) and vertical (bottom) deflectors. The dashed black lines are the results of the simulations.

TABLE IV
RF PARAMETERS FOR THE S-BAND VERTICAL AND HORIZONTAL DEFLECTORS. RF STRUCTURE IS CONSTANT IMPEDANCE AND BACKWARD TRAVELING WAVE

Parameter	Symbol	Value	Unit
RF frequency	f	2998.01	MHz
Length	L	2.466	m
Power-to-voltage	$V/L/P^{0.5}$	2.4	$MV/m/MW^{0.5}$
Wave number	k_{rf}	62.8	m^{-1}
RF input power	P	15	MW
Integrated def. voltage	$V_\perp$	23	MV
Calibration factor	S	3.8/2.8	mm/ps
Temporal resolution	σ_{tR}	13/18	fs
Energy resolution	$\sigma_{\Delta Eind}$	260/190	keV

A. Effect of the Tuning Errors

In order to estimate the effects of the RF tuning errors of the deflector, cell-to-cell phase advance errors were used to estimate electron beam trajectories in the deflector itself. The equation of motion in the vertical plane for each nth cell is

$$\frac{\partial^2 y_n(z)}{\partial z^2} = \frac{eV_\perp}{pcl} \sin\left(\Phi_n + \varphi_{RF}\right) \tag{14}$$

where $\varphi_{RF} = 0$ is the RF phase corresponding to the zero-crossing, l is the length of the deflector, $V_\perp$ is the integrated deflecting voltage, p is the longitudinal momentum of the beam, and Φ_n is the integrated phase error along the structure, as reported in the lower plot of Fig. 16. Fig. 19 shows the effect of the tuning errors on the transverse displacement of the centroid (on the top) and on the angular divergence (at the bottom) as a function of the longitudinal coordinate inside the deflector and for different RF phases. The beam energy is 1.2 GeV and the integrated deflecting voltage is 20 MV. Effects of the tuning errors on the transverse displacement and angular divergence could be quite large if a limit on the integrated phase error is not properly chosen. Residual effects of the tuning error on the phase advance can still be compensated by globally adjusting the RF phase of the deflector system. In this case, the residual kick can be compensated with a RF phase of 1.3 deg and then only an offset of 0.1 mm remains, which is not a severe problem for the measurements.

V. RF POWER DISTRIBUTION AND CONDITIONING

The two deflectors were tested at full available RF power in the FERMI linac using the RF distribution system shown in Fig. 20. In order to use the same klystron for both deflectors, an RF-switch is used to feed one deflector at full RF power at a time. A second RF switch for each deflector is introduced in order to completely attenuate the deflecting fields in the structures, when the second arm of the TH2132A 45 MW klystron is used to feed another accelerating structure at the linac's end. The power test was performed during the FERMI commissioning phase. For both deflectors, the RF conditioning process has been performed with a pulse repetition rate of 10 Hz, by gradually increasing the RF power and the pulse width. This operation started with an RF power lower than 1 MW and with an RF pulse width of 100 ns. When the power is increased for the first time in the waveguides, switches, and deflectors, impurities are released due to the RF heating, causing spikes in the vacuum levels. However, the vacuum system was able to remove the impurities, so that the vacuum levels were always under 10^{-6} mbar. It is worthwhile to note that for the horizontal deflector we reached the RF power of 12 MW with the RF pulse width of 700 ns in the first eight hours of operation. Both deflectors were considered as fully conditioned when it was possible to feed them with a RF power of 15 MW at 2500 ns and with the levels of the vacuum pressure below the threshold of $3 \cdot 10^{-8}$ mbar. This result was reached for both deflectors after approximately 24 hours of operation. Looking at the reflected power from the deflector input, it was possible to count the number of arcs produced by the extraction of electrons from the metallic surface, and consequently to estimate the breakdown rate (BDR). The BDR is the ratio between the number of breakdowns and the number of pulses per RF period during which both the RF power and the width remain constant at fixed values. After 40 hours of conditioning, we estimated the BDR as a function of the pulse width at 15 MW

TABLE V
RF MEASUREMENTS FOR THE VERTICAL (V.) AND HORIZONTAL (H.) DEFLECTORS AT ROOM TEMPERATURE

	Specifications	V. Measured values		H. Measured values	
		Before brazing	After brazing	Before brazing	After brazing
Frequency [MHz]	2998.01	2997.94	2998.09	2997.56	2997.63
SWR	1.0 ÷ 1.1	1.005	1.02	1.007	1.016
Attenuation [Np/m]	0.146	0.208	0.145	0.173	0.158
Filling time [ns]	500	525	521	524	525
Quality factor	13500	9600	13500	11400	12700
$\Delta\varphi$ [°]	120 $\pm$ 1.5	120.22 $\pm$ 0.46	119.85 $\pm$ 0.69	119.93 $\pm$ 0.26	119.82 $\pm$ 0.70

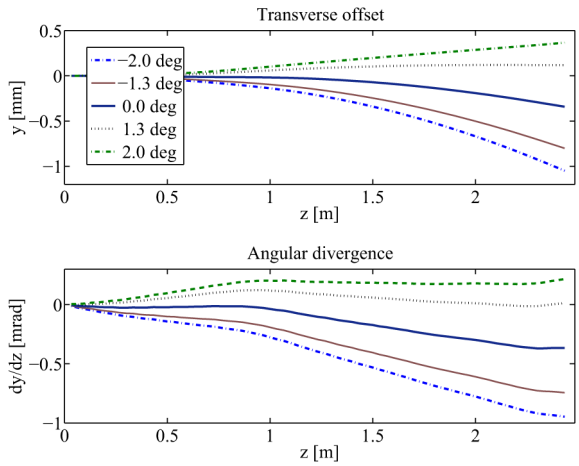

Fig. 19. Effects of the phase advance errors on the transverse displacement of the centroid (up) and on the transverse kick (bottom) as a function of the RF phase.

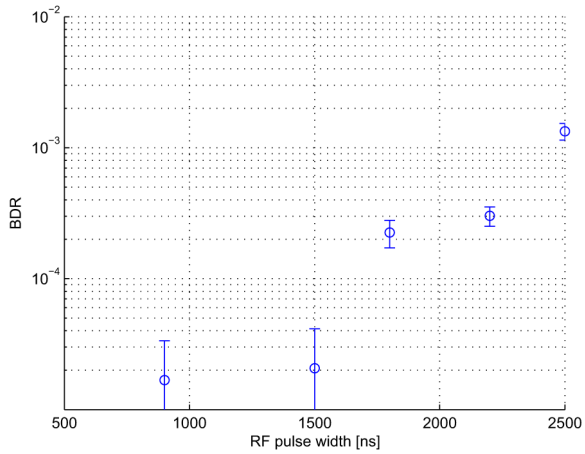

Fig. 21. Breakdown rate of the horizontal deflector as a function of the RF pulse width at fixed RF power of 15 MW.

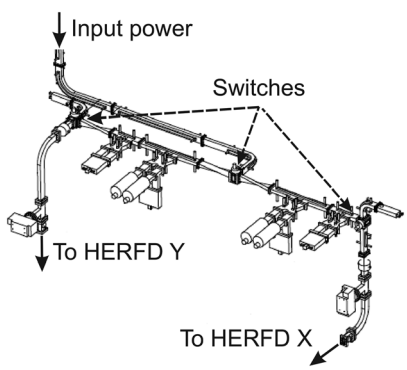

Fig. 20. Waveguide switch system, used to choose the deflection plane.

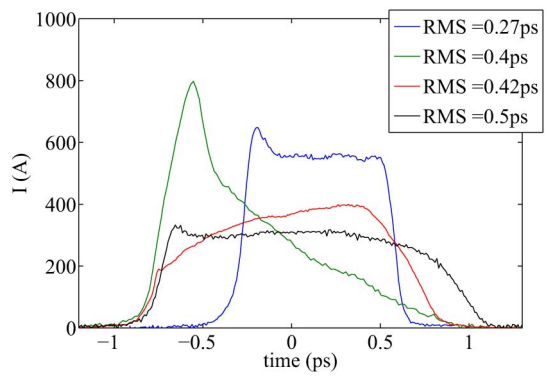

Fig. 22. Electron bunch temporal structure in different machine configurations obtained by activating the vertical deflector and sending the stretched beam to the downstream screen. The head of the bunch is on the left.

for the horizontal deflector. Results are shown in Fig. 21. Since the filling times of the both deflectors are approximately 500 ns, then the RF pulse width was fixed at 900 ns. Such a value ensures a suitable filling of the structures and furthermore the BDR is kept below $2 \cdot 10^{-5}$. It is worthwhile to note that, due to limited RF power and, consequently, low BDR, it was not possible to get the dependence of the BDR on the RF power. The dependence of the BRD on the RF pulse length is clear for high values of RF width, while at low RF widths the structure has very few discharges.

VI. ELECTRON BEAM MEASUREMENTS AND RESULTS

The deflectors have been extensively used to characterize and optimize the electron bunch before entering in the undulator chains both during the commissioning of FERMI FEL-1 and FEL-2 lines either in the routine machine tuning for user's dedicated beam time. Fig. 22 shows the electron current profile and the corresponding bunch length measured with the deflector and imaged on a downstream screen in different machine configurations. When, for instance, the X-band cavity settings are not fully optimized to linearize the compression process, the temporal bunch profile has current spikes in the head (see "green" profile) or in the tail (see "red" profile). As mentioned above, another important beam property that can be diagnosed by the deflectors is the time-sliced emittance. A quadrupole-scan executed after activating the vertical (or alternatively, horizontal)

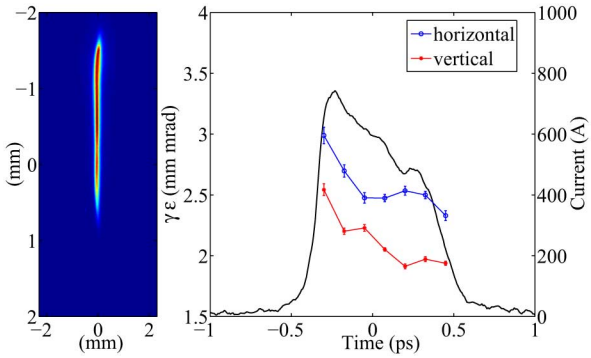

Fig. 23. On the left: vertical deflected beam imaged on the downstream screen; on the right: horizontal (blue line) and vertical (red line) time-sliced emittance measured by using the HERFDy and HERFDx alternatively.

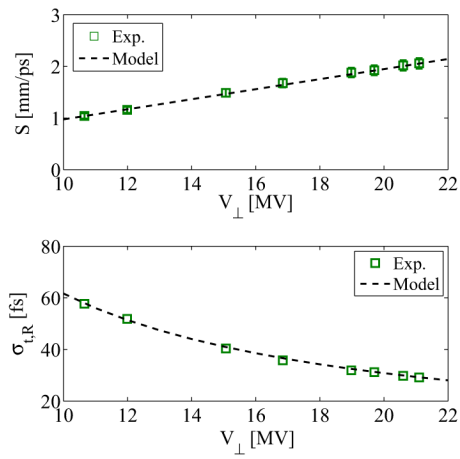

Fig. 24. Calibration factor S (up) and time resolution $\sigma_{t,R}$ (bottom) as a function of the integrated deflecting voltage for the vertical deflector. $E = 1.024$ GeV, $R_{34} = 5.3m$, $\sigma_{y,0} = 60\ \mu m$.

deflector provides a measurement of the horizontal (or alternatively, vertical) slice emittance and Courant-Snyder parameters along the longitudinal bunch coordinate. A typical measurement of time-sliced emittance is reported in Fig. 23. In order to verify RF parameters for the vertical deflector, the time resolution and the calibration factor have been measured as a function of the integrated deflecting voltage, and the results are reported in Fig. 24. There is good agreement between the model and experimental data and the rms time resolution is approximately 30 fs at 21 MV. It is worthwhile noting that in the experiment the angular-to-spatial element R_{34} was just 5.3 m. Using values of the beam optics for the nominal lattice reported in Table I, then the R_{34} will be approximately 10 m providing, through a different setting of the optics, a factor of two better resolution. Finally, combining the vertical deflector with the horizontal bending energy spectrometer provides a measurement of the beam's longitudinal phase space and an example is reported in Fig. 25. This possibility has constituted a valuable advantage in the electron beam optimization. In fact, in an FEL operating in a seeded HGHG mode, the interplay between the electron longitudinal phase space and the seed laser time-frequency dependence plays a crucial role [34], [35] and can strongly influence the final FEL output performance in terms of spectral

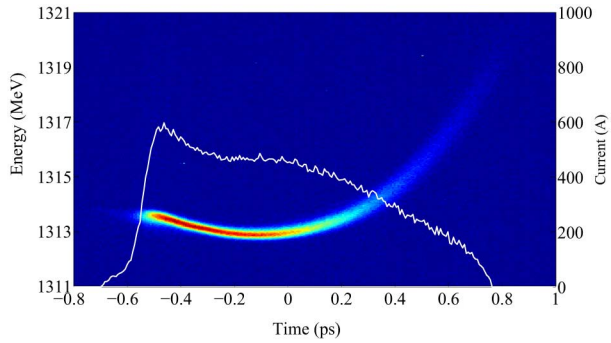

Fig. 25. Longitudinal phase space as measured in the diagnostic beam dump.

purity and intensity. As recently demonstrated [36], [37], controlling and manipulating the longitudinal phase space of the electron bunch can improve the final FEL performance, so it is very important to measure it before sending the bunch through the undulator beam-line. Moreover, micro-bunching instabilities driven by space charge forces and coherent synchrotron radiation occurring during the bunch compressor process and in the linac transport, increase the bunch slice energy spread, thus deteriorating the FEL performance. As is known, a laser heater system can efficiently suppress the micro-bunching instabilities [38]. Measuring the slice energy spread at the end of the linac with this diagnostic equipment has allowed us to efficiently tune the laser heater parameters and minimize the final slice energy spread. Moreover it allowed us to study the impact of the laser heater induced energy spread on the FEL process in the high power regime, thus paving the road of novel FEL concepts [39].

VII. Conclusion

Two high-resolution transverse deflector devices were designed, fabricated, and tested along with their periphery systems and are now in operation for routinely diagnosing the high-energy and high-brightness electron beam for the FERMI. The fabricated 2.5-m long deflectors respectively generate a vertical and horizontal integrated deflecting voltage of 23 MV, and the temporal structure of a compressed beam to hundreds femtoseconds was successful projected on a screen with a calibration factor up to 2 mm/ps. The longitudinal phase-space and slice emittance of the bunch were also successfully measured and analyzed. Furthermore, the knowledge of the slice energy spread at the end of the linac measured with this diagnostic equipment has allowed us to efficiently tune the laser heater parameters in order to suppress micro-bunching instability.

Acknowledgment

The authors would like to thank the Linac, Infrastructure and Vacuum groups for the support in the deflectors installation.

References

[1] W. K. H. Panofsky and W. A. Wenzel, "Some considerations concerning the transverse deflection of charged particles in radio frequency fields," *Rev. Sci. Instrum.*, vol. 27, p. 967, 1956.

[2] R. H. Miller, R. F. Koontz, and D. D. Tsang, "The SLAC Injector," *IEEE Trans. Nucl. Sci.*, vol. 12, no. 3, pp. 804–808, Jun. 1965.

[3] P. R. Phillips, "Microwave separator for high energy particle beams," *Rev. Sci. Instrum.*, vol. 32, pp. 13–16, 1961.

[4] G. A. Loew and O. H. Altenmueller, *Design and Applications of RF Deflecting Structures at SLAC*, PUB-135, Aug. 1965.

[5] H. Hahn and H. J. Halama, "Design of the deflector for the RF beam separator at the Brookhaven AGS," *Rev. Sci. Instrum.*, vol. 36, pp. 1788–1796, 1965.

[6] M. Bell, P. Bramham, and B. W. Montague, "Pulse-shortening in electron linear accelerators and E_{11} type modes," *Nature*, pp. 277–278, 1963.

[7] P. Bernard, H. Lengeler, and V. Vaghin, in *On the Design of Disc-Loaded Waveguides for RF Separators,* CERN Report 68-30, Geneva, Switzerland, 1968.

[8] I. Ben-Zvi, J. X. Qui, and X. J. Wang, "Picosecond-resolution slice emittance measurement of electron-bunches," in *Proc. 1997 Particle Accelerator Conf.*, Vancouver, BC, Canada, 1997.

[9] X. J. Wang, "Producing and measuring small electron bunches," in *Proc. 1999 Particle Accelerator Conf.*, New York, NY, USA, 1999, pp. 229–233.

[10] R. Akre, L. Bentson, P. Emma, and P. Krejcik, "A transverse RF deflecting for bunch length, and phase space diagnostics," in *Proc. 2001 Particle Accelerator Conf.*, Chicago, IL, USA, 2001, pp. 2353–2355.

[11] D. Alesini *et al.*, "RF deflector design and measurements for the longitudinal and transverse phase space characterization at SPARC," *Nucl. Instrum. Meth. Phys. Res.*, Sect. A 568, 488, 2006.

[12] S. Korepanov *et al.*, "An RF deflector for the longitudinal, and transverse beam phase space analysis at PITZ," in *Proc. 2007 Diagnostics and Instrumentation for Particle Accelerator Conf.*, Venice, Italy, 2007, TUPB32.

[13] M. Rohrs, C. Gerth, H. Schlarb, B. Schmidt, and P. Schmuser, "Time-resolved electron beam phase space tomography at soft x-ray free-electron laser," *Phys. Rev. ST Accel. Beams*, vol. 12, p. 050704, 2009.

[14] Y. Ding *et al.*, "Femtosecond x-ray pulse temporal characterization in free-electron lasers using a transverse deflector," *Phys. Rev. ST Accel. Beams*, vol. 14, p. 120701, 2011.

[15] C. Behrens *et al.*, "Few-femtosecond time-resolved measurements of X-ray free-electron lasers," *Nat. Commun.*, vol. 5, article no. 3762, 2014.

[16] E. Allaria *et al.*, "Highly coherent and stable pulses from a seeded free-electron laser in the extreme ultraviolet," *Nat. Photon.*, vol. 6, pp. 699–704, 2012.

[17] E. Allaria *et al.*, "Two-stage seeded soft-X-ray free-electron laser," *Nat. Photon.*, vol. 7, pp. 913–918, 2013.

[18] S. Di Mitri *et al.*, "Design and simulation challenges for FERMI@Elettra," *Nucl. Instrum. Meth. Phys. Res.*, Sect. A 608, 19, 2009.

[19] P. Craievich, S. Di Mitri, M. Ferianis, M. Veronese, D. Alesini, and M. Petronio, "A transverse RF deflecting cavity for the FERMI@Elettra project," in *Proc. 2007 Diagnostics and Instrumentation for Particle Accelerator Conf.*, Venice, Italy, 2007, p. 168.

[20] R. L. Brown, "A first- and second-order matrix theory for the design of beam transport systems and charged particle spectrometers," *SLAC-Report*, p. 75, 1982.

[21] C. Behrens and Ch. Gerth, "On the limitations of longitudinal phase space measurements at high-gain free-electron lasers using a transverse deflecting structure," in *Proc. 2009 Diagnostics and Instrumentation for Particle Accelerator Conf.*, Basel, Switzerland, 2009, TUPB44.

[22] D. Alesini *et al.*, "Sliced beam parameter measurements," in *Proc. 2009 Diagnostics and Instrumentation for Particle Accelerator Conf.*, Basel, Switzerland, 2009, TUOA01.

[23] M. Minty and F. Zimmermann, "Beam techniques - beam control and manipulation," *Proc. Lectures Given at the US Particle Accelerator School, University of Chicago and Argonne National Laboratory(1999)*, 2003, SLAC-R-621.

[24] G. Penco *et al.*, "Time-sliced emittance and energy spread measurements at FERMI@Elettra," in *Proc. 2012 Free Electron Laser Conf.*, Nara, Japan, 2012, p. 417.

[25] V. A. Dolgashev, G. Bowden, Y. Ding, P. Emma, P. Krejcik, J. Lewandowski, C. Limborg, M. Litos, J. Wang, and D. Xiang, "Design and application of multimegawatt X-band deflectors for femtosecond electron beam diagnostics," *Phys. Rev. ST Accel. Beams*, vol. 17, p. 102801, 2014.

[26] L. Faillace *et al.*, "X-band travelling wave deflector for ultra-fast beam diagnostics," in *Proc. 2010 Int. Particle Accelerator Conf.*, Kyoto, Japan, 2010, p. 1206.

[27] H. Ego, H. Maesaka, Y. Otake, T. Sakurai, T. Hashirano, and S. Miura, "Transverse C-band deflecting structure for longitudinal phase space diagnostics in the XFEL/SPring-8 SACLA," in *Proc. 2011 International Particle Accelerators Conf.*, San Sebastian, Spain, 2011, pp. 1221–1223.

[28] O. H. Altenmueller, R. R. Larsen, and G. A. Loew, "Investigations of traveling-wave separators for the Stanford two-mile linear accelerator," *Rev. Sci. Instrum.*, vol. 35, pp. 438–442, 1964.

[29] H. Hahn, "Deflecting mode in iris-loaded waveguides," *Rev. Sci. Instrum.*, vol. 34, pp. 1094–1100, 1963.

[30] P. Bernard, H. Lengeler, and V. Vaghin, in *New Disk-Loaded Waveguides for the CERN RF Separator,* CERN Report 70-26, Geneva, Switzerland, 1970, .

[31] [Online]. Available: http://www.ansoft.com/products/hf/hfss/

[32] D. Alesini *et al.*, "Design of couplers for traveling wave RF structures using 3D electromagnetic codes in the frequency domain," *Nucl. Instrum. Meth. Phys. Res.*, Sect. A 580, no. 3, pp. 1176–1183, 2007.

[33] R. B. Neal, General Editor, The Stanford Two-Mile Accelerator Stanford Univ.. Stanford, CA, USA, 1968.

[34] A. A. Lutman, G. Penco, P. Craievich, and J. Wu, "Impact of an initial energy chirp and an initial energy curvature on a seeded free electron laser: The greens function," *J. Phys. A: Math. Theory*, vol. 42, p. 045202, 2009.

[35] A. A. Lutman, G. Penco, P. Craievich, and J. Wu, "Impact of an initial energy chirp and an initial energy curvature on a seeded free electron laser: Free electron laser properties," *J. Phys. A: Math. Theory*, vol. 42, p. 085405, 2009.

[36] G. Penco *et al.*, "Experimental demonstration of electron longitudinal-phase-space linearization by shaping the photoinjector laser pulse," *Phys Rev. Lett.*, vol. 112, p. 044801, 2014.

[37] P. Emma *et al.*, "Experimental demonstration of energy-chirp control in relativistic electron bunches using a corrugated pipe," *Phys Rev. Lett.*, vol. 112, p. 034801, 2014.

[38] Z. Huang *et al.*, "Measurements of the linac coherent light source laser heater and its impact on the x-ray free-electron laser performance," *Phys. Rev. ST Accel. Beams*, vol. 13, p. 020703, 2010.

[39] E. Ferrari *et al.*, "Impact of non-Gaussian electron energy heating upon the performance of a seeded free-electron laser," *Phys. Rev. Lett.*, vol. 112, p. 114802, 2014.